Aerosol-Jet-Printed Encapsulation of Organic Photovoltaics

Robin Basu, Kok S. Siah, Andreas Distler, Felix Häußler, Jörg Franke,
Christoph J. Brabec, and Hans-Joachim Egelhaaf*

Organic electronic devices (OEDs) are prone to oxygen- and water-induced
degradation and therefore need to be encapsulated with barrier materials. In this
work, an aerosol jet (AJ)-printing process is developed to coat perhydropolysi-
lazane (PHPS) directly onto OEDs by adapting the print setup and systematically
optimizing the process parameters. Furthermore, a novel curing process that
converts PHPS to silica barrier layers is developed by combining damp heat (DH)
exposure with subsequent vacuum–UV irradiation. This two-step treatment is
shown to be considerably faster and gentler than the state-of-the-art curing
processes and also yields a quantitatively higher conversion. Both the printing
and the conversion process are fully compatible with OED devices, which is
demonstrated by a damage-free direct encapsulation of organic solar cells. The
encapsulated cells show a significant reduction of degradation in DH conditions
(65 °C/85% r.h.), maintaining >95% of their initial performance for >100 h.
Complementary electroluminescence measurements reveal that the AJ-printed
barrier layers effectively prevent lateral water ingress into the devices. Herein, the
proof of principle is provided that AJ printing can be used to print barrier layers
directly onto OEDs and is thus an industrially highly relevant technology to
precisely encapsulate such devices even on 3D objects.

1. Introduction

Organic solar cells (OSCs) have gained sig-
nificant attention in recent years due to
their potential for low-cost, flexible, and
lightweight photovoltaics.[1] Another signif-
icant advantage of OSCs over most other
photovoltaics is their printability, that is,
processability from solution. This
allows not only for large-scale roll-to-roll
processing on flexible substrates, but also
for additive manufacturing via inkjet or
aerosol jet (AJ) printing, for example, on
3D objects.[2–8]

However, a major issue of OSCs is their
sensitivity to moisture and oxygen, which
can lead to significant degradation in per-
formance over time.[9,10] Encapsulation of
the solar cells protects them from the envi-
ronment and improves their long-term
stability. Thus, the quality of the barrier
determines the lifetime of these organic
electronic devices (OEDs).[11] As their
lifetime also has a direct impact on the
respective levelized cost of electricity, a
high stability minimizes the overall costs and is thus especially
important for the market competitiveness of organic PV.[12,13]
It has been reported that a water vapor transmission rate of
$10^{-3}\,g\,m^{-2}\,d^{-1}$ at 25 °C and 40% relative humidity can be suffi-
cient to ensure OSC lifetimes of three to five years.[11,14,15]
In addition, a proper encapsulation as a passive component of
the device should not compromise the intrinsic properties of
OSCs. Ideally, a proper barrier material for these photovoltaics
should be flexible, optically transparent, lightweight, and cost
efficient.[12,14,16]

For example, when being laminated between glasses, which
provide a perfect encapsulation against extrinsic factors, the
OSCs' benefits of lightweight and flexibility get lost.
Therefore, a sandwich lamination between transparent barrier
foils, which usually comprise multilayer stacks of Al_2O_3 or
SiO_2 in combination with organic films, using a UV-curing epoxy
glue is the current state-of-the-art encapsulation for flexible solar
modules.[17] However, such barrier foils are very expensive, as
their fabrication involves a time-consuming process and a mul-
titude of coatings under vacuum.[15] Moreover, for the protection
of OEDs on 3D objects with curved surfaces, classical encapsu-
lation by lamination is no longer an option. In this and also
other cases, printing the barrier layers directly onto the device
constitutes a highly interesting approach to reduce weight, thick-
ness, and cost of the final device.[18] In addition to composite

R. Basu, A. Distler, C. J. Brabec, H.-J. Egelhaaf
Friedrich-Alexander-Universität Erlangen-Nürnberg (FAU)
Faculty of Engineering
Department of Material Science
Materials for Electronics and Energy Technology (i-MEET)
Martensstraße 7, 91058 Erlangen, Germany
E-mail: andreas.distler@fau.de

K. S. Siah, F. Häußler, J. Franke
Friedrich-Alexander-Universität Erlangen-Nürnberg (FAU)
Faculty of Engineering
Department Mechanical Engineering
Institute for Factory Automation and Production Systems (FAPS)
Egerlandstraße 7-9, 91058 Erlangen, Germany

C. J. Brabec, H.-J. Egelhaaf
Forschungszentrum Jülich GmbH (FZJ)
Helmholtz-Institute Erlangen-Nürnberg (HI-ERN)
Immerwahrstraße 2, 91058 Erlangen, Germany

(iD) The ORCID identification number(s) for the author(s) of this article
can be found under https://doi.org/10.1002/adem.202300322.

materials based on nano-clays[19] or glass flakes,[20] perhydropolysilazane (PHPS) has been used as printed encapsulant due to its high capability of blocking the ingress of moisture and oxygen.[10,21–24]

PHPS is a nontoxic and low-cost material that is also widely used as barrier coating for passivating steel or silicon surfaces (including photovoltaics).[25–28] The backbone of this inorganic polymer class consists of silicon and nitrogen atoms ($SiNH_2$-NH) and thus can be converted to silica by exposure to water vapor or reactive oxygen species.[29] Hence, this material is suitable to form dense, homogenous, and defect-free silica films from solution-based processes.[30]

In this article, we investigate the potential of AJ-printed PHPS layers for encapsulating OSCs. AJ printing is a noncontact, mask-free printing method that utilizes an AJ to deposit uniform layers of precise geometries onto different substrates.[31–35] This method is frequently used for printed electronics and has the advantage of being able to print onto a wide range of substrates, including flexible ones, and curved or even 3D surfaces.[33,34,36,37] The high lateral resolution of this technique will allow the selective encapsulation of those parts of OEDs, which are sensitive to environmental factors, without affecting other parts of the circuit, especially electrical contacts.

Here, we develop and optimize an AJ-printing process for depositing PHPS layers. We evaluate the performance and stability of both, the barrier layers themselves as well as the encapsulated OSCs devices. The developments are precisely described, which include adjustments to the printing setup and optimization of process parameters to obtain the best-possible topology of printed barrier layers and complete coverage of the solar cells upon encapsulation. We further elaborate a novel process to convert PHPS to silica with extraordinarily high conversion rates in very short times without harming the underlying OSC. Overall, for the first time, the results of this work present an industrially highly relevant process to directly encapsulate OSCs by AJ printing, which can also be applied to 3D surfaces.

2. Results and Discussion

2.1. Printing Process Development and Optimization

2.1.1. AJ Print Setup

For the sake of printing PHPS onto arbitrary (including 3D) objects with high lateral resolution and good thickness control, we chose AJ printing and adapted a commercially available AJ printer to our needs (**Figure 1**a).

The base AJ setup with a marathon sprint deposition head from Optomec, Inc. consists of a pneumatic atomizer, a solution reservoir, a sheath gas and exhaust hose, a virtual impactor, and a deposition head with a nozzle (300 μm opening). For printing of finely defined structures, a shutter can be attached. This assembly is mounted into a 5-axis kinematic system from Neotech AMT, which allows printing in three dimensions, that is, onto 3D objects.

Some special modifications are made to the setup to enable printing of PHPS. Instead of the softer and cheaper ethylene propylene diene monomer rubber o-rings, the chemically more stable fluorine rubber o-rings are used to give the gas stream pathway a better seal, which reduces instabilities and hence allows for a more homogenous print. Another issue with PHPS is that it immediately starts to precipitate as soon as some of the solvents evaporate, resulting in nozzle clogging and blocking of the gas flow from the atomizer to the nozzle. To prevent this, a bubbler filled with di-n-butyl ether (the solvent of the PHPS formulation) is added to the flow path, which ensures saturation of the gas stream with the solvent, to avoid any clogging of the system. Finally, accumulation of large droplets of PHPS on the nozzle is observed for longer printing durations, which is likely due to condensation of solvent in the hose connecting the virtual impactor and the print head. Such droplets may lead to nozzle clogging and inhomogeneous printing, which is why a droplet catcher is added to the printing setup. The substrate is placed on a plate that can rotate in all directions, which allows
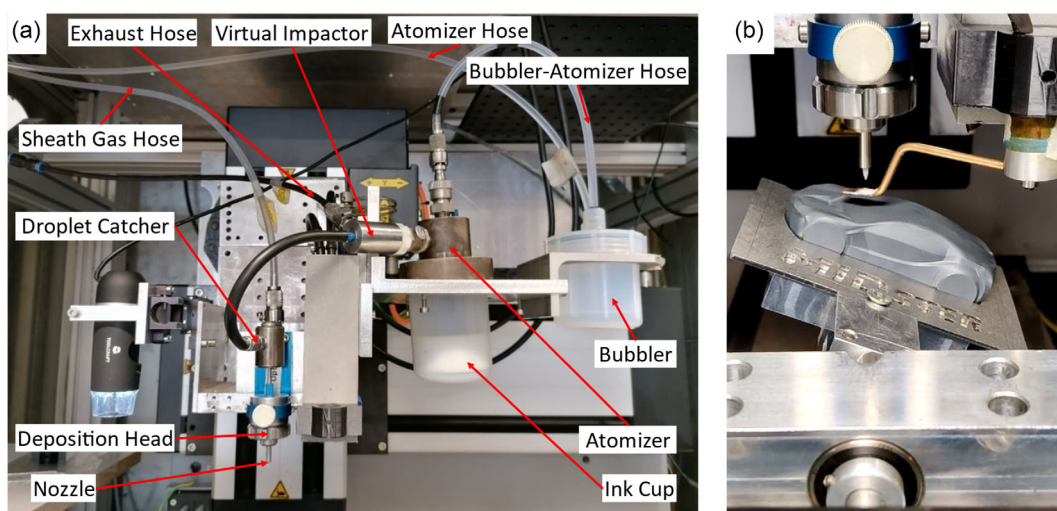

Figure 1. a) Aerosol jet (AJ) printer with modifications for perhydropolysilazane (PHPS) printing and b) printing onto a 3D object.

**ADVANCED
SCIENCE NEWS**

www.advancedsciencenews.com

**ADVANCED
ENGINEERING
MATERIALS**

www.aem-journal.com

for 3D-printing, and the addition of a shutter allows selectively interrupted printing (Figure 1b).

2.1.2. Influence of PHPS Solution Formulation and Printing Parameters

Since defects and inhomogeneities in the PHPS layer will have an effect on its barrier properties, the quality of the printed layers needs to be examined and optimized by adapting the PHPS solution formulation as well as the printing parameters.

One major issue that limits the homogeneity of PHPS prints with an AJ is the "coffee ring effect" (CRE). The CRE is the result of inhomogeneous evaporation over the area of droplets on a surface. Higher evaporation rates at the edges of the droplets result in a solute dragging flow of solvent toward them, which creates a ring-like shape of the dried droplet that is typically observed from coffee stain.[38] Consequently, an AJ-printed line will exhibit increased thickness toward its edges, as shown in **Figure 2**a,b. To quantify the CRE, we introduce a "CRE index" ψ that represents the ratio of the highest thickness of the edges to the lowest thickness between them, that is, $\psi = h_{max}/h_{min}$. This allows for quantitative comparability over a large variety of printing parameters. In this work, ψ was determined by scanning the profiles of a printed line at 100 positions with a confocal microscope and taking the average value.

While areas with insufficient layer thickness will directly limit the barrier properties of the PHPS layer, areas with excessive layer thickness may evoke crack formation[9] or prevent complete transformation of the PHPS layer to SiO_2 due to incomplete penetration of the curing agents into the printed line, which in turn impairs the barrier properties negatively as well. Consequently, uniform coating over the entire print area is necessary for achieving good barrier layers. Therefore, the influence of different printing parameters on ψ are investigated and optimized to reduce it to unity.

2.1.3. Printing of Single Lines

The basic optimization of printing parameters is performed by printing and examining individual lines of PHPS onto glass substrates. There are three gas flow rates of importance for AJ printing (see **Figure 3**): the atomizer flow rate (AFR), or carrier gas flow rate, determines the amount of aerosol that is
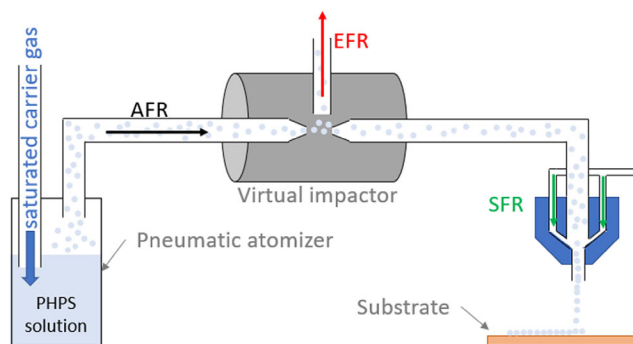
Figure 3. Schematic drawing of the AJ-printing setup and process, indicating the atomizer flow rate (AFR, black), the exhaust flow rate (EFR, red), and the sheath flow rate (SFR, green).

transferred from the atomizer to the deposition head. The exhaust flow rate (EFR) is generated by the virtual impactor and determines the particle size distribution in the aerosol. The sheath flow rate (SFR) affects the focus of the gas stream that is directed to the substrate.[39]

The first step of optimization is to adjust AFR and EFR for a PHPS solution that was diluted 1:1 with di-n-butyl ether as proposed by Channa et al.[10] for blade coating. The threshold for material deposition is an AFR of $700 \, cm^3 \, min^{-1}$, if the sheath gas flow is turned off (i.e., SFR = 0). Dependent on the AFR, there is a threshold for the EFR, above which no material is deposited onto the substrate. The correlation of EFR and AFR is measured and plotted in **Figure 4**a.

The AFR for all following printing experiments is set to $1000 \, cm^3 \, min^{-1}$, at which the upper limit for printing is an EFR of $500 \, cm^3 \, min^{-1}$. It is noteworthy that the upper limit of the EFR can vary by around 10% for each printing procedure, because it is highly dependent on a good sealing as well as ink properties (e.g., viscosity). By reducing the applied EFR by $20 \, cm^3 \, min^{-1}$ below its upper limit, the risk of potential interruptions of material deposition due to process fluctuations is effectively reduced (see Figure S1, Supporting Information, for a more detailed correlation of EFR and line properties). In addition, such slightly lower EFR is also found to reduce the CRE index ψ of printed lines in some cases, which can be seen in Figure 4b. This plot also shows the dependence of ψ on the SFR for different EFRs. The lowest CRE index is observed for
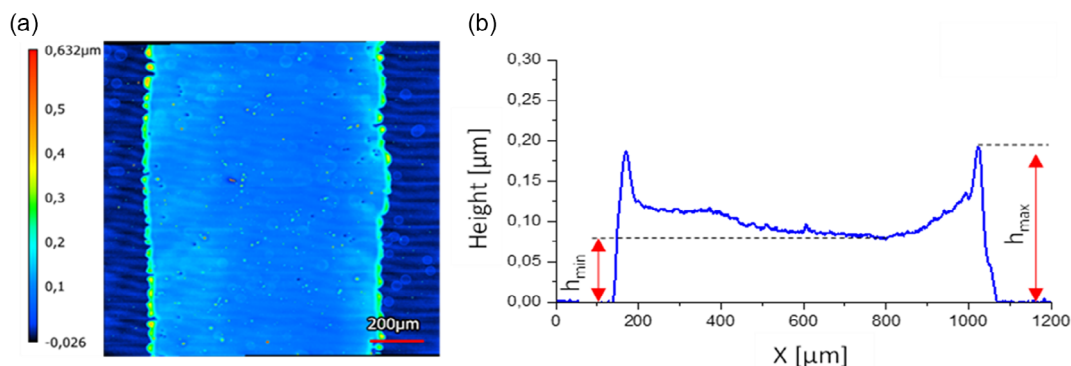
Figure 2. a) Confocal microscope image and b) averaged height profile over 100 cross-sectional lines of an AJ-printed PHPS line on glass.
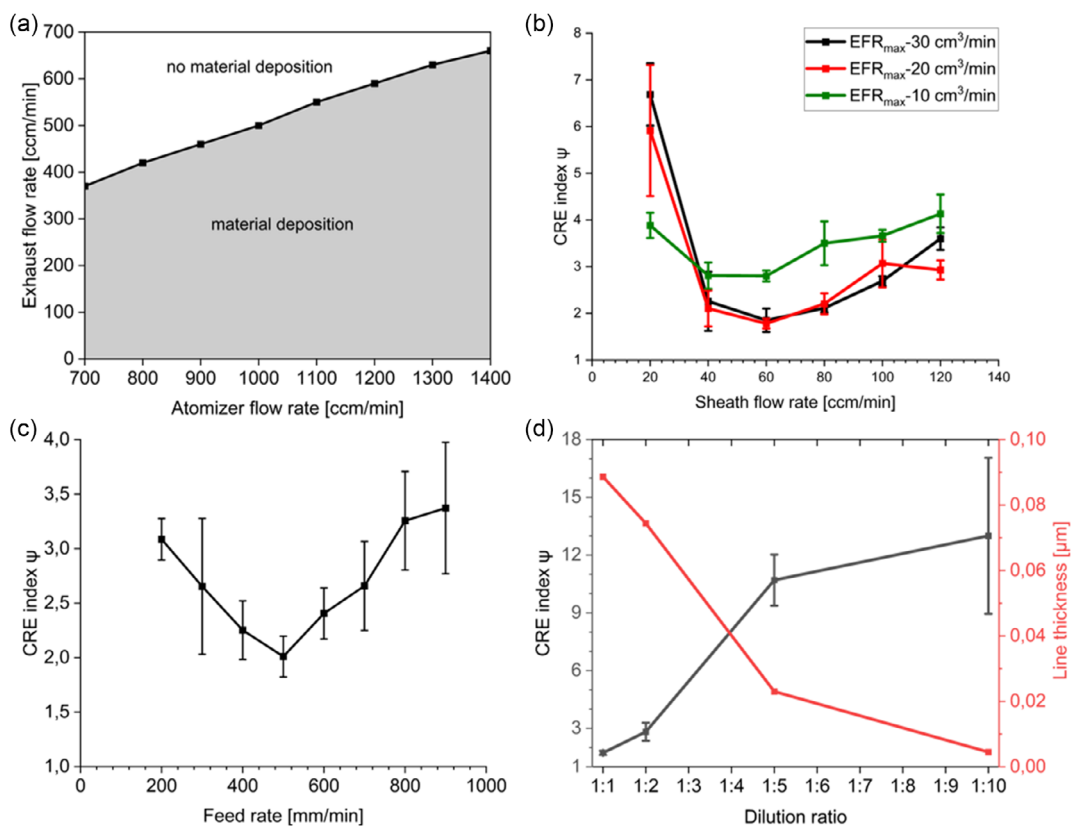
Figure 4. Optimization of the AJ-printing process: a) upper limits for the EFR at different AFR; b) coffee ring effect (CRE) index ψ of printed lines in dependence of the SFR for EFRs 10, 20, and 30 cm^3 min^{-1} below its upper limit EFR$_{max}$ (500 cm^3 min^{-1}); c) CRE index of printed lines in dependence of the substrate feed rate (FR); and d) dependence of CRE index and line thickness on the dilution ratio of PHPS solution with di-n-butyl ether.

values of ERF of 20 and 30 cm^3 min^{-1} below the upper limit and for values of SFR of 60 cm^3 min^{-1}, while lower and higher SFRs increase ψ, and hence decrease the homogeneity of the printed lines. This may be explained by the fact that, on one hand, a decreasing SFR generally leads to an increased volume of deposited material (see Figure S2, Supporting Information), which prolongs the drying time of the deposited droplets and in turn enhances the CRE.[40,41] On the other hand, the increase of ψ with increasing SFR at values beyond 60 cm^3 min^{-1} may relate to the deposited material being blown to the line edges by the increased intensity of the sheath gas flow, as previously reported by Tait et al.[42]

Finally, the feed rate (FR) of the substrate also influences the appearance of printed lines (see Figure 4c). The FR is an equivalent for the printing speed and equals the distance covered per minute (at constant material deposition rate), that is, the higher the FR, the less material is deposited on the substrate. Consequently, lower FRs correlate with a higher volume of deposited material and thus longer drying times, which favors the CRE, as described before (see Figure S3, S4, Supporting Information, for a more detailed correlation of FR and line properties). In contrast, too high FRs will result in rough surfaces or even incomplete coverage of the intended areas. The results of our optimization show that the best trade-off, that is, the lowest CRE index, is achieved using an FR of 500 mm min^{-1}.

Finally, since concentrated PHPS solutions start to chemically react under ambient conditions (light, air, and humidity) already within a couple of minutes and in turn lead to clogging of the nozzle during printing, the PHPS solution is diluted with di-n-butyl ether. Consequently, higher dilution rates allow for longer printing durations. However, increasing the dilution also results in thinner and more inhomogeneous prints, which is shown in Figure 4d. For dilution ratios higher than 1:1, the line quality is found to decrease drastically, becoming too thin and inhomogeneous for the intended application. As a result, the best trade-off between process stability and quality of the layer is a dilution ratio of 1:1, which allows for process durations of at least 1 h.

At this point, it is to note that we optimized the process parameters regarding the functionality of the PHPS as a barrier layer, that is, aiming for the highest homogeneity possible, since too thick and/or uneven layers become rigid and may form cracks (as shown in Figure S5, Supporting Information) and thus lose their barrier properties, as already reported in the literature.[10] With our optimized parameter set that reaches the lowest CRE, the line width of the AJ-printed PHPS line is $\approx$1 mm. While it would be possible to further increase or decrease the line width, this would be at the cost of homogeneity (see Figure S6, Supporting Information), and for our application the individual line width is not a key parameter.

**ADVANCED
SCIENCE NEWS**

www.advancedsciencenews.com

**ADVANCED
ENGINEERING
MATERIALS**

www.aem-journal.com

2.1.4. Printing of Areas

For printing a 2D area with PHPS, several lines are printed next to each other with a certain degree of overlapping. This degree of overlapping is defined by the "stepover," a value that represents the overlap between adjacent lines. For 100% stepover, the lines are edge to edge (i.e., no overlap), and for a stepover of 50%, the distance between the center of two lines is half the line width. Due to the CRE, this results in an alternating hill–valley topography (see **Figure 5**a).

The lower the stepover is, the thicker the resulting layers are, but also the higher ψ gets, as can be seen in Figure 5b. Both too thick PHPS layers as well as too high ψ values increase the probability of crack formation in the layer (as mentioned in the previous chapter), which impairs the barrier functionality. The lowest CRE is found for a stepover of 50%, while too high stepover values increase the probability of holes in the layer, which also leads to bad barrier properties.

Printing two of such layers on top of each other (without intermittent curing) results in no significant improvement of the CRE index (see Figure 5c), instead, it only results in a proportionally higher roughness of the PHPS layer.

To conclude, based on the previously described optimizations, we managed to reduce the CRE to a minimum with ψ values down to 1.9 and 3.4 for single lines and areas, respectively. The respective printing parameters are summarized in **Table 1** and are used for the following experiments. The UV/vis spectrum of such PHPS layers shows a transmission of $\approx$100% over the whole spectral range (see Figure S7, Supporting Information), that is, no optical losses are expected if photovoltaic devices are irradiated through PHPS barrier layers.

It is to note that it would certainly be desirable to further decrease the CRE value close to 1, which was however not possible with our setup, since especially the low concentration of the PHPS ink that is needed not to clog the nozzle in our setup unfortunately leads to an increased roughness of the layer (see Figure 4d). Consequently, an optimization of the printing ink in terms of different solvent systems would be one approach to further decrease the roughness of the layers. Furthermore, there are other aspects that could be investigated to potentially further reduce the topographical variation, for example, to investigate the effect of different nozzle diameters or geometries (e.g., flat nozzle). A wider nozzle enables printing

Table 1. Overview of optimized parameter settings for aerosol jet printing of PHPS.

Processing Parameter	Processing Value
Temperature	Room temperature
PHPS dilution	1:1
Atomizer flow rate (AFR)	1000 cm^3 min
Exhaust flow rate (SFR)	480 cm^3 min
Sheath flow rate (EFR)	60 cm^3 min
Feed rate	500 mm min
Stepover (for areas)	50%

of wider line profiles at an appropriate material deposition rate, which could potentially improve the overall surface homogeneity, as fewer lines are required to cover the desired area. Finally, a more extensive investigation of the interaction between the different printing parameters by means of design of experiment could provide more insight into the process window and could yield potential improvement of the achievable layer homogeneity.

2.2. Encapsulation of Solar Cells

After printing PHPS, the layer needs to be cured (i.e., converted to silicon dioxide) to provide proper barrier properties. This can be done either by exposure to damp heat (DH) or by vacuum–UV (V–UV) irradiation with an excimer lamp) under oxygen-containing environments.[43] In our case, DH curing was performed at 65 °C/85% relative humidity and V–UV irradiation was done with a xenon excimer lamp ($\lambda_{emission}(Xe_2^*) = 172$ nm) in air with a lamp-sample distance of 5 mm. The conversion can be verified and quantified by infrared spectroscopy. Upon conversion, the peaks corresponding to stretching vibrations of N–H (3400 cm^{-1}), Si–H (2150 cm^{-1}), and Si–N (830 cm^{-1}) decrease and eventually disappear, while new peaks of Si–O at 450 cm^{-1} (bending vibration) and 1050 cm^{-1} (stretching vibration) appear and increase in the spectrum.[43,44] This is shown in **Figure 6**a for a PHPS film being cured by V–UV light for 1 min, which shows no significant conversion to SiO$_2$ yet, and for 5 min, where conversion to SiO$_2$ is clearly detectable. The ratio of the peaks at 1050 and 830 cm^{-1} can therefore be
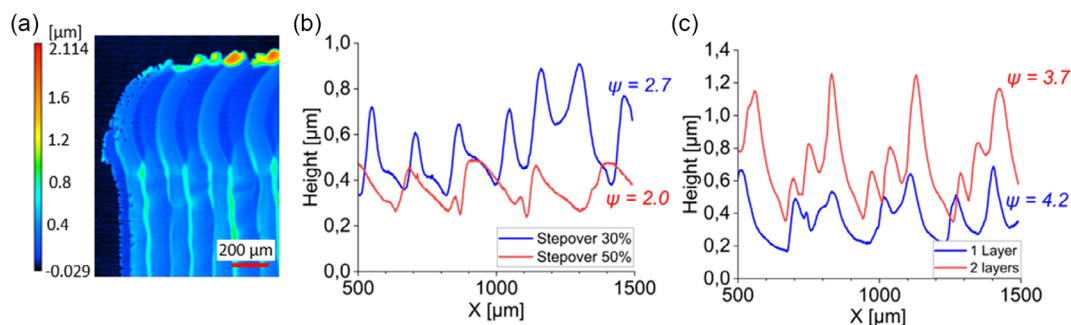

Figure 5. a) Confocal microscope image of an AJ-printed PHPS pad, b) comparison of height profiles of cured PHPS layers printed with 30% (blue) and 50% (red) stepover, and c) comparison of the height profiles double- (red) and single-layer (red) pads for a stepover of 50%.
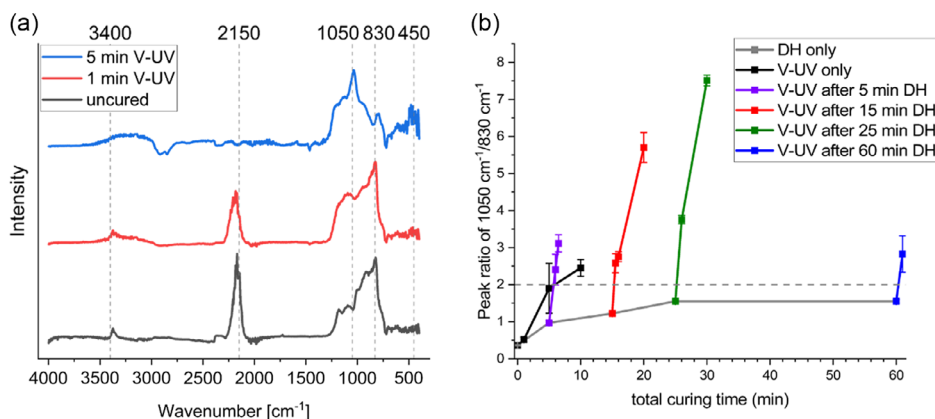
Figure 6. Curing of PHPS under different conditions: a) change in infrared peak intensities during curing (vacuum–UV [V–UV]). b) Changes in ratio of peaks at 1050 and 830 cm^{-1} upon curing with V–UV only (black), with damp heat (DH) only (grey), and for a two-step curing process of V–UV irradiation after different exposure times to DH (colored).

used to determine the quality of the curing process. According to Channa et al., a peak ratio of two and higher indicates sufficient curing for the purpose of encapsulation. For a sufficiently high conversion ratio of PHPS to silica by V–UV curing only, it is necessary to expose the layers for at least 10 min to V–UV (see Figure 6b). However, OSCs of the layer stack glass/indium tin oxide (ITO)/ZnO (N10)/PM6:Y6:PC$_{61}$BM/MoO$_3$/Ag being exposed to such conditions, suffer severe damage, especially when being unprotected, but also when bearing a printed layer of PHPS on top, which can be seen in Figure S8a, Supporting Information. In areas where no PHPS is printed, strong oxidation of the silver top electrode is observed, but also some parts that were covered with PHPS exhibit small-area damages after V–UV curing. The respective power conversion efficiency (PCE) of the cells shows a relative decrease of 70.9% and 17.8% for the bare cells and the PHPS-protected ones, respectively.

As can be seen in Figure 6b, this peak ratio threshold is surpassed after 10 min of V–UV curing (black data), whereas with DH curing the peak ratio remains below two even after 60 min of curing (grey data). Consequently, the conversion rate of PHPS is lower under DH compared to V–UV irradiation. This is in accordance with the literature and the reason, why in most cases, V–UV curing is the preferred curing method.[43] However, if the encapsulation is printed directly onto an OED, the highly energetic V–UV irradiation and the formed reactive oxygen species may potentially damage the subjacent OED, a problem that has already been discussed in the literature.[22,45]

To reduce the resulting damage, we employ a two-step process that combines the two curing methods. The first step consists in initial curing under DH conditions, which is expected to be less harmful to the OED. The second curing step is performed by V–UV irradiation, which is known to provide more complete conversion. The silica layer that is created during the first curing step is intended to prevent potential photooxidation during the V–UV exposure of the second process step and thus reduce damage to the device. Surprisingly, with this two-step process, we find that much higher peak ratios than for the two individual methods can be achieved in even shorter time (see colored curves in Figure 6b).[10] For example, the combination of 25 min DH

exposure and subsequent 5 min of V–UV irradiation result in a peak ratio of 7.5.

The reason for this extreme increase in conversion ratio is not fully understood yet. Possibly, humidity permeates further into uncured PHPS before reacting with the polymer than the reactive oxygen species formed by V–UV irradiation, thus creating silanol groups throughout the layer. To complete the conversion to silica, it is necessary to apply heat that causes condensation of the silanol groups.[46] While complete condensation is not achieved at 65 °C, the following V–UV irradiation has been reported to effectively support the conversion.[43]

When using our newly developed two-step curing procedure for converting PHPS to silica, the devices need to be exposed to V–UV for only 90 s (after 60 min DH pre-curing) to be fully cured. In this case, no visible damage of devices with a PHPS layer on top is observed (see Figure S8b, Supporting Information). The gentleness of the two-step process is further confirmed by current–voltage (I–V) measurements after each process step. **Table 2** shows the average photovoltaic performance of all devices, before encapsulation, after application of a PHPS layer by AJ printing, after pre-curing in DH for 60 min, and after subsequent V–UV curing for 60 min. Remarkably, the performance of the devices was not impaired over the complete process. This means that the two-step curing process allows for high-conversion ratios of ≥2 and at the same time is not harmful to the OSCs.

Table 2. Changes in short-circuit current (J_{SC}), open-circuit voltage (V_{OC}), fill factor (FF), and power conversion efficiency (PCE) of solar cells (averaged over 40 devices) with the layer stack glass/ITO/N10/PM6:Y6: PC$_{61}$BM/Poly(3,4-ethylenedioxythiophene) (PEDOT):F/Ag before encapsulation, after aerosol jet (AJ) printing of PHPS, after the initial damp heat (DH) curing, and after the final V–UV curing.

Process step	J_{SC} [mA cm^{-2}]	V_{OC} [V]	FF [%]	PCE [%]
0. Before encapsulation	23.4 ± 1.1	0.80 ± 0.01	61.4 ± 3.0	11.4 ± 0.8
1. AJ printing	23.5 ± 1.2	0.80 ± 0.01	61.7 ± 4.8	11.6 ± 1.1
2. DH pre-curing	23.6 ± 1.3	0.79 ± 0.02	60.5 ± 5.3	11.3 ± 1.4
3. V–UV curing	23.5 ± 1.1	0.79 ± 0.01	61.5 ± 2.9	11.4 ± 0.8

2.3. Measurement and Optimization of Barrier Properties

To investigate the AJ-printed layers regarding their protection against water vapor transmission, encapsulated OSCs of the layer stack glass/ITO/ZnO (N10)/PM6:Y6:PC$_{61}$BM/Poly(3,4-ethylene-dioxythiophene) (PEDOT):F/Ag are subjected to a degradation test in DH (65 °C/85% relative humidity). Under these conditions, OSCs comprising PEDOT-based hole-transport layers are known to undergo severe degradation due to the hygroscopicity of the PEDOT, featured by the increase of series resistance, and thus can be used as a probe for water ingress into the devices.[47] For AJ-encapsulated solar cells, the two-step encapsulation process described in Chapter 2.2.1 is used, while unencapsulated cells serve as reference. The initial performances (before degradation) of the unencapsulated and AJ-encapsulated solar cells are listed in Table 2.

Figure 7a depicts the evolution of device performance during the course of degradation inside the climate chamber. After 137 h, the unencapsulated cells have lost 81% of their initial PCE, while the AJ-encapsulated cells still maintain almost their full initial performance (only 4% loss). The respective current density–voltage (J–V) curves of the cells (Figure 7b,c) indicate water ingress as the culprit for the deterioration of the unencapsulated cell.[47] While the open-circuit voltage (V_{OC}) remains stable, the fill factor (FF) significantly drops due to an increased series resistance and the commencing formation of a second diode ("S-shape"). For the unencapsulated devices, the FF drops to 51% of its initial value, whereas the FF of the encapsulated devices only drops slightly (see Figure S9, Supporting Information). These results clearly show that the AJ-printed PHPS barriers significantly slow down the water vapor transmission into the solar cells.

To retrace the way of water ingress into the devices upon DH degradation, electroluminescence (EL) images of fresh and degraded devices are taken. Each substrate contains six individual solar cells, two of which have not been encapsulated and four have been encapsulated with PHPS by AJ-printing prior to DH exposure, as shown in the device layout in **Figure 8**a.

Figure 8b shows the EL image of the solar cells before degradation. All active cell areas light up homogeneously, and with the same intensity, independently of whether being encapsulated or not, which is in-line with the equal initial device efficiency of all cells. Upon degradation, all cells lose in overall EL intensity (see Figure 8c), which is in accordance with the observed drop of current injection at the bias of +1.5 V that is applied for EL imaging (Figure 7b,c). However, the AJ-encapsulated devices (bottom four cells) still show a homogeneous EL signal over the whole active layer with hardly any "dark spots." On the contrary, the unencapsulated devices (two top cells) show large inactive areas or even complete device failure, which is attributed to local ingress of water.[47] Since the dark spots are not homogenously distributed over the cell area, as can be seen in the top left cell, but rather are all connected to one or two edges of the cell, it is very likely that the degradation of the unencapsulated devices is due to lateral water ingress underneath the Ag top electrode. This behavior is effectively suppressed by the AJ encapsulation of the devices.
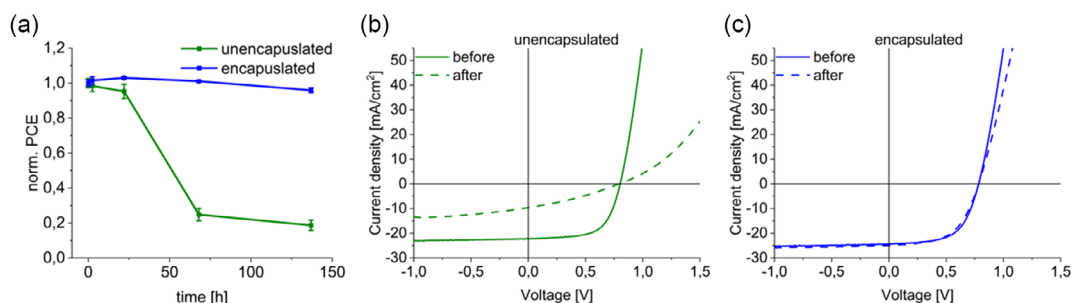

Figure 7. a) Normalized power conversion efficiency (PCE) of solar cells with the layer stack glass/indium tin oxide (ITO)/N10/PM6:Y6:PC61BM/PEDOT:F/Ag without (green) and with (blue) AJ-printed encapsulation upon DH degradation (65 °C/85% r.h.). b,c) Graphs of current density versus external bias (J–V curves) of a representative b) unencapsulated and c) an AJ-encapsulated cell before (solid lines) and after (dashed lines) 137 h of degradation.
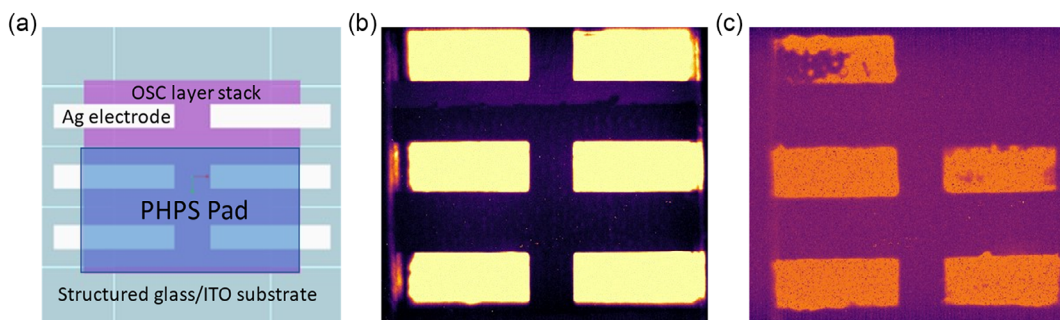

Figure 8. a) Schematic drawing of the device layout of a substrate bearing both unencapsulated (top two) and AJ-encapsulated (bottom four) solar cells. Electroluminescence images of such devices at an applied voltage of 1.5 V b) before and c) after DH degradation.

**ADVANCED
SCIENCE NEWS**

www.advancedsciencenews.com

**ADVANCED
ENGINEERING
MATERIALS**

www.aem-journal.com

3. Conclusions

A process for encapsulating OSCs with PHPS by means of AJ printing has been developed. This process can be used to protect printed electronics on both 2D as well as 3D surfaces from water and oxygen. Our optimized PHPS solution formulation and printing parameters enable stable printing for at least 1 h and provide homogeneous prints. Furthermore, the newly developed two-step curing process for the conversion of PHPS to silicon dioxide by combining DH exposure and subsequent V–UV irradiation has been shown to transform the PHPS faster and more quantitatively in comparison to both individual curing processes and is thus of high interest for industrial application. In addition, both the printing and the conversion process are fully compatible with OEDs, which enables their encapsulation by printing the barrier layer directly on top of the device without causing any performance losses. Applying this approach to a production environment, OEDs can be encapsulated in-line by using the same printing techniques as used for the device fabrication itself, which saves time and cost for additional materials and machinery (e.g., for encapsulation by lamination). Finally, utilizing AJ printing for applying the barrier allows for a selective and precise encapsulation of water- and oxygen-sensitive OEDs on any kind of substrate, including 3D objects with curved surfaces.

4. Experimental Section

Materials: ITO-coated glass substrates with a sheet resistance of $15\,\Omega\,\square^{-1}$ were purchased from VisionTek. PHPS in the form of a 20 wt% solution in di-n-butyl ether was purchased from durXtreme GmbH, Germany. ZnO (N-10; 2.5 wt% in isopropanol [IPA]) was purchased from Avantama, Switzerland. Poly[(2,6-(4,8-bis(5-(2-ethylhexyl-3-fluoro) thiophen-2-yl)-benzo[1,2-b:4,5-b0]dithiophene))-alt-(5,5-(10,30-di-2-thienyl-50,70-bis(2-ethylhexyl)benzo[10,20-c:40,50-c0]dithiophene-4,8-dione)] (PBDB-T-2F, aka "PM6") and (2,20 -((2Z,20 Z)-((12,13-bis (2-ethyl-hexyl)-3,9-diundecyl-12,13-dihydro-[1,2,5]thiadiazolo[3,4-e]thieno[200 300: 40,50]thieno[20,30:4,5]pyrrolo[3,2-g]thieno[20,30 :4,5]thieno[3,2-b]indole-2,10-diyl)bis (methanylylidene))-bis(5,6-difluoro-3-oxo2,3-dihydro-1H-indene-2,1-diylidene))dimalononitrile) ("Y6") were purchased from Derthon OPV; [6,6]-phenyl-C61-butyric acid methyl ester (PC60BM) was purchased from Solenne. PEDOT:F was obtained by Prof. Yinhua Zhou's research group at the Wuhan National Laboratory for Optoelectronics, Huazhong University of Science and Technology, China. The active layer, the hole-transport layer, and electron-transport layer of the OSC devices were produced by doctor blading (ZAA 2300, manufactured by Zehntner Testing Instruments, Switzerland). The PHPS films were printed with a Marathon Sprint AJP system from Optomec, Inc. with a pneumatic atomizer.

OSC Fabrication: Prestructured glass/ITO substrates were cleaned in an ultrasonic bath in IPA and blown dry. Subsequently, a layer of zinc oxide (N-10, Avantama) was coated onto the substrate with a doctor blade (coating speed: $5\,\mathrm{mm\,s^{-1}}$). Before annealing, the ZnO at 120 °C for 30 min in air excess material was removed from the bottom contact areas. PM6:Y6:PC$_{61}$BM (0.9:1:0.1) was used as active layer material. The coating parameters were adjusted, so that the optical density of the films was around 0.5–0.6. The layer was annealed for 10 min at 110 °C inside a nitrogen-filled glove box. PEDOT:F was blade-coated on top with $10\,\mathrm{mm\,s^{-1}}$ without subsequent annealing. The top electrode consisted of 246 nm thick evaporated silver. The resulting cell area was 0.1 cm^2.

Characterization Methods: Fourier-transform infrared spectroscopy spectra of PHPS samples were recorded with an Alpha II system from Bruker in attenuated total reflection (ATR) mode operating the OPUS/IR 7.2 software. The profiles of printed encapsulations were measured with a Keyence VK-X3050—3D laser scan microscope. Accelerated lifetime tests to determine the effect of AJ-printed PHPS barriers on the lifetime of OSC devices were performed under well-controlled conditions. The encapsulation was carried out as described in Chapter 2.2.2. The substrates with encapsulated and unencapsulated OSCs were positioned in a climate chamber (ESPEC LHL-144), with the preset condition of 65 °C at 85% relative humidity following the standardized DH test protocol for organic photovoltaics (ISOS–D–3).[48] C–V characteristics and PCEs of the solar cells were measured during the ageing experiments by an LOT solar simulator (Class AAA) at $100\,\mathrm{mW\,cm^{-2}}$. For this purpose, the solar cells were taken out of the climate chambers and put back after the measurement. To analyze degradation by light, the encapsulated P3HT films were placed under continuous irradiation in ambient air in the chamber of a SUNTEST XXL+ sun simulator (Atlas Materials Testing Technology GmbH) with daylight filter. The light source was a Xenon lamp with an irradiation intensity set to $60\,\mathrm{W\,m^{-2}}$ in the range of 300–400 nm. The chamber temperature was kept at 40 °C, while the black-body temperature was 65 °C. Changes in the UV–Vis spectra during degradation were investigated using a Shimadzu UV-1800 spectrometer. Crack formation was observed with an Olympus MX51 optical microscope. The EL images of degraded and undegraded cells were taken with a Ninox VIS-SWIR 640 camera from Raptor Photonics with an air-cooled extended indium–gallium–arsenide detector (InGaAs) upon excitation with a Keysight B2901A Precision Source/Measure Unit from Keysight Technologies, Inc.

Supporting Information

Supporting Information is available from the Wiley Online Library or from the author.

Acknowledgements

Conflict of Interest

The authors declare no conflict of interest.

Data Availability Statement

The data that support the findings of this study are available from the corresponding author upon reasonable request.

Keywords

[1] L. Lucera, P. Kubis, F. W. Fecher, C. Bronnbauer, M. Turbiez, K. Forberich, T. Ameri, H.-J. Egelhaaf, C. J. Brabec, *Energy Technol.* **2015**, *3*, 373.

[2] D. Corzo, K. Almasabi, E. Bihar, S. Macphee, D. Rosas-Villalva, N. Gasparini, S. Inal, D. Baran, *Adv. Mater. Technol.* **2019**, *4*, 1900040.

[3] M.-K. Hamjah, M. Steinberger, K. C. Tam, H.-J. Egelhaaf, C. J. Brabec, J. Franke, in *2021 14th Int. Congress Molded Interconnect Devices (MID)*, IEEE, Piscataway, NJ **2021**, p. 1.

[4] J. Hoerber, J. Glasschroeder, M. Pfeffer, J. Schilp, M. Zaeh, J. Franke, *Procedia CIRP* **2014**, *17*, 806.

[5] M. Smith, Y. S. Choi, C. Boughey, S. Kar-Narayan, *Flexible Printed Electron.* **2017**, *2*, 15004.

[6] D. Graf, S. Neermann, L. Stuber, M. Scheetz, J. Franke, in *2018 13th Int. Congress Molded Interconnect Devices (MID)*, IEEE, Piscataway, NJ **2018**, p. 1.

[7] S. Martin, M. Himmler, A. Bruns, S. Reitelshöfer, D. Pham, D. W. Schubert, J. Franke, in *Electroactive Polymer Actuators and Devices (EAPAD) XXIII* (Eds: J. D. Madden, I. A. Anderson, H. R. Shea), SPIE, Bellingham, Washington (USA) **2021**, p. 58.

[8] L. Tu, S. Yuan, H. Zhang, P. Wang, X. Cui, J. Wang, Y.-Q. Zhan, L.-R. Zheng, *J. Appl. Phys.* **2018**, *123*, 174905.

[9] M. Jørgensen, K. Norrman, S. A. Gevorgyan, T. Tromholt, B. Andreasen, F. C. Krebs, *Adv. Mater.* **2012**, *24*, 580.

[10] I. A. Channa, A. Distler, M. Zaiser, C. J. Brabec, H.-J. Egelhaaf, *Adv. Energy Mater.* **2019**, *9*, 1900598.

[11] J. A. Hauch, P. Schilinsky, S. A. Choulis, S. Rajoelson, C. J. Brabec, *Appl. Phys. Lett.* **2008**, *93*, 103306.

[12] G. Dennler, C. Lungenschmied, H. Neugebauer, N. S. Sariciftci, M. Latrèche, G. Czeremuszkin, M. R. Wertheimer, *Thin Solid Films* **2006**, *511–512*, 349.

[13] S. A. Gevorgyan, I. M. Heckler, E. Bundgaard, M. Corazza, M. Hösel, R. R. Søndergaard, G. A. dos Reis Benatto, M. Jørgensen, F. C. Krebs, *J. Phys. D: Appl. Phys.* **2017**, *50*, 103001.

[14] J. Ahmad, K. Bazaka, L. J. Anderson, R. D. White, M. V. Jacob, *Renewable Sustainable Energy Rev.* **2013**, *27*, 104.

[15] M. Giannouli, V. M. Drakonakis, A. Savva, P. Eleftheriou, G. Florides, S. A. Choulis, *Chemphyschem* **2015**, *16*, 1134.

[16] P. Burrows, G. Graff, M. Gross, P. Martin, M. Shi, M. Hall, E. Mast, C. Bonham, W. Bennett, M. Sullivan, *Displays* **2001**, *22*, 65.

[17] L. J. Sutherland, H. C. Weerasinghe, G. P. Simon, *Adv. Energy Mater.* **2021**, *11*, 2101383.

[18] I. A. Channa, A. Distler, C. J. Brabec, H.-J. Egelhaaf, *Organic Flexible Electronics*, Elsevier, Sawston, Cambridge (UK) **2021**, p. 249.

[19] A. D. Chandio, I. A. Channa, M. Rizwan, S. Akram, M. S. Javed, S. H. Siyal, M. Saleem, M. A. Makhdoom, T. Ashfaq, S. Khan, S. Hussain, M. D. Albaqami, R. G. Alotabi, *Coatings* **2021**, *11*, 942.

[20] I. A. Channa, A. Distler, B. Scharfe, S. Feroze, K. Forberich, B. Lipovšek, C. J. Brabec, H.-J. Egelhaaf, *Flexible Printed Electron.* **2021**, *6*, 25006.

[21] D. Kim, G. G. Jeon, J. H. Kim, J. Kim, N. Park, *ACS Appl. Mater. Interfaces* **2022**, *14*, 34678.

[22] J. Kim, J. H. Jang, J.-H. Kim, K. Park, J. S. Jang, J. Park, N. Park, *ACS Appl. Energy Mater.* **2020**, *3*, 9257.

[23] L. Sun, K. Uemura, T. Takahashi, T. Yoshida, Y. Suzuri, *ACS Appl. Mater. Interfaces* **2019**, *11*, 43425.

[24] L. Prager, U. Helmstedt, H. Herrnberger, O. Kahle, F. Kita, M. Münch, A. Pender, A. Prager, J. W. Gerlach, M. Stasiak, *Thin Solid Films* **2014**, *570*, 87.

[25] H. Nagayoshi, H. Sakakibara, *EC PVSEC Proc.* **2013**, https://doi.org/10.4229/28thEUPVSEC2013-2DV.3.38.

[26] F. Riffard, E. Joannet, H. Buscail, R. Rolland, S. Perrier, *Oxid. Met.* **2017**, *88*, 211.

[27] N. Yang, W. Wang, W. Cai, K. Lu, *Corros. Sci.* **2020**, *177*, 108946.

[28] P. Colombo, G. Mera, R. Riedel, G. D. Sorarù, *J. Am. Ceram. Soc.* **2010**, *93*, 1805.

[29] A. Lukacs, *J. Am. Ceram. Soc. Bull.* **2007**, *86*, 9301.

[30] H. J. Seul, H.-G. Kim, M.-Y. Park, J. K. Jeong, *J. Mater. Chem. C* **2016**, *4*, 10486.

[31] C. Goth, S. Putzo, J. Franke, in *Sixty First Electronic Components & Technology Conf.*, IEEE, Piscataway, NJ May–June **2011**, p. 1211.

[32] M.-K. Hamjah, J. Zeitler, Y. Eiche, L. Lorenz, C. Backhaus, G.-A. Hoffmann, A. Wienke, S. Kaierle, L. Overmeyer, N. Lindlein, K. Bock, J. Franke, in *2021 14th Inter. Congress Molded Interconnect Devices (MID)*, IEEE, Piscataway, NJ **2021**, p. 1.

[33] E. B. Secor, *Flexible Printed Electron* **2018**, *3*, 35002.

[34] W. Verheecke, M. Dyck, F. Vogeler, A. Voet, H. Valkenaers, *8th Int. DAAAM Baltic Conf. "INDUSTRIAL ENGINEERING"*, Tallinn, Estonia **2012**, pp. 373–379.

[35] N. J. Wilkinson, M. A. A. Smith, R. W. Kay, R. A. Harris, *Int. J. Adv. Manuf. Technol.* **2019**, *105*, 4599.

[36] J. M. Hoey, A. Lutfurakhmanov, D. L. Schulz, I. S. Akhatov, *J. Nanotechnol.* **2012**, *2012*, 324380.

[37] M. Sukeshini A., F. Meisenkothen, P. Gardner, T. L. Reitz, *J. Power Sources* **2013**, *224*, 295.

[38] R. D. Deegan, *Phys. Rev. E: Stat. Phys. Plasmas Fluids Relat. Interdiscip. Top.* **2000**, *61*, 475.

[39] *Image-Based Quality Indices of Aerosol Jet Printed Conductive Lines* (Eds: K. Wang, Y.-H. Chang, C. Zhang, B. Wang), SAMPE Tech, Wichita, Kansas (USA) **2013**.

[40] X. Shen, C.-M. Ho, T.-S. Wong, *J. Phys. Chem. B* **2010**, *114*, 5269.

[41] G. L. Goh, S. Agarwala, W. Y. Yeong, *ACS Appl. Mater. Interfaces* **2019**, *11*, 43719.

[42] J. G. Tait, E. Witkowska, M. Hirade, T.-H. Ke, P. E. Malinowski, S. Steudel, C. Adachi, P. Heremans, *Org. Electron.* **2015**, *22*, 40.

[43] L. Prager, A. Dierdorf, H. Liebe, S. Naumov, S. Stojanović, R. Heller, L. Wennrich, M. R. Buchmeiser, *Chemistry* **2007**, *13*, 8522.

[44] A. Morlier, S. Cros, J.-P. Garandet, N. Alberola, *Thin Solid Films* **2014**, *550*, 85.

[45] L. Sun, Y. Kurosawa, H. Ito, Y. Makishima, H. Kita, T. Yoshida, Y. Suzuri, *Org. Electron.* **2019**, *64*, 176.

[46] A. Morlier, S. Cros, J.-P. Garandet, N. Alberola, *Thin Solid Films* **2012**, *524*, 62.

[47] J. Adams, M. Salvador, L. Lucera, S. Langner, G. D. Spyropoulos, F. W. Fecher, M. M. Voigt, S. A. Dowland, A. Osvet, H.-J. Egelhaaf, C. J. Brabec, *Adv. Energy Mater.* **2015**, *5*, 1501065.

[48] M. O. Reese, S. A. Gevorgyan, M. Jørgensen, E. Bundgaard, S. R. Kurtz, D. S. Ginley, D. C. Olson, M. T. Lloyd, P. Morvillo, E. A. Katz, A. Elschner, O. Haillant, T. R. Currier, V. Shrotriya, M. Hermenau, M. Riede, K. R. Kirov, G. Trimmel, T. Rath, O. Inganäs, F. Zhang, M. Andersson, K. Tvingstedt, M. Lira-Cantu, D. Laird, C. McGuiness, S. Gowrisanker, M. Pannone, M. Xiao, J. Hauch, et al., *Sol. Energy Mater. Sol. Cells* **2011**, *95*, 1253.